30th Symposium on Naval Hydrodynamics
Hobart, Australia, 2-7 November 2014

Large Eddy Simulation of Sheet to Cloud Cavitation

Aswin Gnanaskandan and Krishnan Mahesh
(University of Minnesota, USA)

ABSTRACT

Large eddy simulation on unstructured grids is used to study sheet to cloud cavitation over a wedge. The multiphase medium is represented using a homogeneous equilibrium model that assumes thermal equilibrium between the liquid and the vapor phase. The governing equations are the compressible Navier Stokes equations for the liquid/vapor mixture along with a transport equation for the vapor mass fraction. The solution method is based on the unstructured finite volume algorithm of Park and Mahesh (2007). A characteristic-based filtering scheme is developed to handle shocks and contact discontinuities in non-ideal gases and mixtures. A filter is applied as a corrector step in a predictor-corrector approach with the predictor scheme being non-dissipative and symmetric. The method, validated for a one dimensional problem and a leading edge cavitation problem over a hydrofoil is then applied to study sheet to cloud cavitation over a wedge.

INTRODUCTION

Cavitation refers to the formation of vapor when pressure in a liquid drops below vapor pressure. It occurs in a wide variety of situations such as valves, orifices and propulsor blades. The formation of vapor is often followed by a growth of the vapor cavity and its violent collapse under high pressure. The physical consequences of this collapse include noise, vibration and surface erosion. A cavitating flow contains a wide range of length and time scales. Vapor cavities of various sizes can form and collapse at different rates which makes their prediction very challenging.

Numerical methods to simulate multiphase flows can be broadly classified into two categories : Lagrangian and Eulerian methods. In the Lagrangian method (Unverdi and Tryggvason (1992); Popinet and Zaleski (1999)), the movement of the fluid interface is tracked by introducing a secondary moving grid. Although this approach best resolves the interface, a three dimensional implementation of this method can be complicated. The Eulerian method has no moving grids (Hirt and Nichols (1981); Youngs (1982); Osher and Fedkiw (2003, 2001)) and the interface is obtained by solving for a separate scalar function. Two different approaches are used within the Eulerian method - the multi fluid (Saurel and Lemetayer (2001); Coquel et al. (1997); Saurel and Abgrall (1999)) and the single fluid models (Liu et al. (2004); Saito et al. (2007); Seo and Lele (2009); Seo et al. (2008)). In the multi fluid model, the governing equations are solved separately for each fluid phase and mass, momentum and energy transfer are handled via source terms. The single fluid model treats the mixture of different fluids as a single compressible fluid. In order to close this system, a constitutive equation of state is defined for the mixture. This paper uses the single fluid model.

A turbulent cavitating flow has a broadband spectrum which in our opinion requires non dissipative numerical schemes to represent small scales accurately. However, non-dissipative schemes can become unstable at high Reynolds numbers. Furthermore, cavitation is characterized by large gradients in density and strong pressure waves formed during vapor cloud collapse. Capturing these large discontinuities can be achieved by either adding a filter or by using upwind schemes. In this study we consider the filtering technique, since a filter can be implemented as a corrector step to a base predictor scheme (Ghosh and Mahesh (2008)). The characteristic-based filtering method uses a non-linear filter to provide different amounts of dissipation to the equations, based on the magnitude of the jump. This method was developed for ideal gases on structured grids by Yee et al. (1999) and extended to ideal gases on unstructured grids by Park and Mahesh (2007). In this paper, we develop a characteristic based filtering method for multiphase cavitating flows on unstructured grids.

Sheet to cloud cavitation causes severe damage to the structure when the cloud collapses. Several experiments have been conducted to understand the sheet to cloud transition mechanism. Arndt

et al. (2000) studied a NACA 0015 hydrofoil and observed two types of behaviour based on the parameter $\frac{\sigma}{2\alpha}$, where σ is the cavitation number and α is the angle of attack. They concluded that a re-entering jet was responsible for cavity destabilization for $\frac{\sigma}{2\alpha} > 4$, while at values less than that, a bubbly shock dominates the mechanism. The former was called as Type I instability, whereas the latter was Type II. Leroux et al. (2004) observed a quasi stable partial sheet cavity for cavity lengths less than half the chord length and sheet to cloud cavitation for lengths greater than half the chord length. They also agreed with the conclusions of Arndt et al. (2000) but modified the parameter as $\frac{\sigma}{2(\alpha-\alpha_0)}$, where α_0 is zero for symmetric hydrofoils. Callenaere et al. (2001) established the importance of an adverse pressure gradient at the cavity closure for the formation of a re-entering jet. They observed two types of cavity, thick and thin based on the amount of interaction between the re-entering jet and the cavity interface. For thick cavities, the interaction between the re-entering jet and the cavity is minimum until the re-entering jet reaches the leading edge of the cavity, giving rise to the classical sheet to cloud transition. On the other hand, in a thin cavity, the interaction with re-entering jet causes the cavity to split into many small structures. In this case, though the cavity does not auto oscillate, the re-entering jet is still periodic with a Strouhal number in the range 0.2 - 0.4. Kubota et al. (1992) also observed a cloud cavity that formed due to shear layer instability of the cavity interface, where the role of a re-entering jet was found to be small. Laberteaux and Ceccio (2001) further classified the cavities as open and closed based on the absence and presence of re-entering jet respectively. A closed cavity has a clear interface and a re-entering jet is often found, whereas an open cavity is typically frothy with no clear re-entering jet. Thus several mechanisms have been proposed for cavity destabilization. This paper is organized as follows. Section "Governing Equations" outlines the governing equations along with the source terms for evaporation of water and condensation of vapor. Section "Numerical method" discusses the predictor-corrector algorithm along with the spatial and temporal discretization schemes. The characteristic based filtering applied as a corrector step is also discussed in this section. Validation cases and sheet to cloud cavitation over a wedge are discussed in section "Results" and a brief summary in section "Summary" concludes the paper.

GOVERNING EQUATIONS

We use a homogeneous equilibrium model that assumes thermal and mechanical equilibrium between the phases i.e. there is no slip velocity or temperature difference between the phases. Surface tension effects are ignored and the constituent phases are treated as a single compressible fluid whose density is given by

$$\rho = \rho_l(1-\alpha) + \rho_g\alpha, \tag{1}$$

where ρ_l is the density of liquid and ρ_g is the density of vapor. α is the vapor volume fraction which is related to the vapor mass fraction by

$$\rho_l(1-\alpha) = \rho(1-Y) \quad \text{and} \quad \rho_{\mathrm{g}}\alpha = \rho \mathrm{Y}. \tag{2}$$

The governing equations are the Navier-Stokes equations along with a transport equation for the mass fraction of vapor:

$$\begin{aligned}
\frac{\partial \rho}{\partial t} &= -\frac{\partial}{\partial x_k}\left(\rho u_k\right), \\
\frac{\partial \rho u_i}{\partial t} &= -\frac{\partial}{\partial x_k}\left(\rho u_i u_k + p\delta_{ik} - \sigma_{ik}\right), \\
\frac{\partial \rho e_s}{\partial t} &= -\frac{\partial}{\partial x_k}\left(\rho e_s u_k - Q_k\right) - p\frac{\partial u_k}{\partial x_k} + \sigma_{ik}\frac{\partial u_i}{\partial x_k} \\
\frac{\partial \rho Y}{\partial t} &= -\frac{\partial}{\partial x_k}\left(\rho Y u_k\right) + S_e - S_c,
\end{aligned} \tag{3}$$

where ρ, u_i, e_s and p are density, velocity, internal energy and pressure respectively of the mixture.

$$\begin{aligned}
\rho e_s &= \rho_l e_l(1-\alpha) + \rho_g e_g \alpha, \text{ where} \\
e_l &= C_{vl}T + \frac{P_c}{\rho_l} \text{ and } \mathrm{e_g = C_{vg}T} \\
\rho e_s &= \rho C_{vm}T + \rho(1-Y)\frac{P_c K_l}{p+P_c}, \\
E_T &= \rho e_s + \frac{1}{2}\rho u_k u_k.
\end{aligned} \tag{4}$$

Here, e_l and e_g are the internal energies of liquid and gas respectively. C_{vl} and C_{vg} are the specific heats at constant volume for liquid and vapor respectively while C_{pl} and C_{pg} are the specific heats at constant pressure. The system is closed using a mixture equation of state.

$$p = Y\rho R_g T + (1-Y)\rho K_l T\frac{p}{p+P_c}, \tag{5}$$

Here, $R_g = 461.6$ J/KgK, $K_l = 2684.075$ J/KgK and $P_c = 786.333$ x 10^6 are constants associated with the equation of state of vapor and liquid. Since internal energy is a function of both pressure and temperature, we need to obtain these variables using energy

equation and equation of state. Solving these two equations simultaneously leads to a quadratic equation $ap^2 + bp + c = 0$, where

$$\begin{aligned} a &= C_{vm}, \\ b &= C_{vm}P_c + (1-Y)P_cK_l - \\ &\quad [(1-Y)K_l + YR_g]\rho e_s, \\ c &= -YR_gP_c\rho e_s. \end{aligned} \tag{6}$$

Now pressure is obtained as the positive root of this quadratic and then temperature is computed from Eq. (5). The viscous stress σ_{ij} and heat flux Q_i are given by

$$\begin{aligned} \sigma_{ij} &= \mu\left(\frac{\partial u_i}{\partial x_j} + \frac{\partial u_j}{\partial x_i} - \frac{2}{3}\frac{\partial u_k}{\partial x_k}\delta_{ij}\right), \\ Q_i &= k\frac{\partial T}{\partial x_i}, \end{aligned} \tag{7}$$

where the mixture viscosity and mixture thermal conductivity are defined as

$$\begin{aligned} \mu &= \mu_l(1-\alpha)(1+2.5\alpha) + \mu_g\alpha, \\ k &= k_l(1-\alpha) + k_g\alpha. \end{aligned} \tag{8}$$

To perform LES, the Eqs. (3) are spatially filtered which gives additional filtering terms: SGS stress, SGS heat flux and SGS scalar dissipation. These terms are modeled using a Dynamic Smagorinsky model (DSM).

$$\begin{aligned} \tau_{ij} - \frac{\delta_{ij}}{3}\tau_{kk} &= -2C_S(\mathbf{x},t)\overline{\rho}\Delta^2\left|\tilde{S}\right|\widetilde{S^*_{ij}}, \\ \tau_{kk} &= 2C_I(\mathbf{x},t)\overline{\rho}\Delta^2\left|\tilde{S}\right|^2, \\ q_i &= -\overline{\rho}\frac{C_S(\mathbf{x},t)\Delta^2\left|\tilde{S}\right|}{Pr_T}\frac{\partial\overline{T}}{\partial x_i}, \\ t_i &= -\overline{\rho}\frac{C_S(\mathbf{x},t)\Delta^2\left|\tilde{S}\right|}{Sc_T}\frac{\partial\overline{Y}}{\partial x_i}, \end{aligned} \tag{9}$$

where $|S| = \sqrt{2S_{ij}S_{ij}}$ and $S^*_{ij} = S_{ij} - 1/3S_{kk}\delta_{ij}$. Model coefficients C_s, C_I, Pr_T and Sc_T are determined by the Germano identity. For example,

$$\begin{aligned} C_S\Delta^2 &= \frac{1}{2}\frac{\langle L^*_{ij}M^*_{ij}\rangle}{\langle M^*_{ij}M^*_{ij}\rangle}, \\ L^*_{ij} &= \left(\frac{\widehat{\overline{\rho u_i}\cdot\overline{\rho u_j}}}{\overline{\rho}}\right) - \frac{\widehat{\overline{\rho u_i}}\cdot\widehat{\overline{\rho u_j}}}{\widehat{\overline{\rho}}}, \\ M^*_{ij} &= \widehat{\overline{\rho}\left|\tilde{S}\right|\widetilde{S^*_{ij}}} - \widehat{\overline{\rho}}\left(\frac{\widehat{\Delta}}{\Delta}\right)^2\widehat{\left|\tilde{S}\right|}\widehat{\widetilde{S^*_{ij}}}, \end{aligned} \tag{10}$$

where, $\langle\cdot\rangle$ denotes spatial average over homogeneous direction(s) and the caret denotes the test filtering.

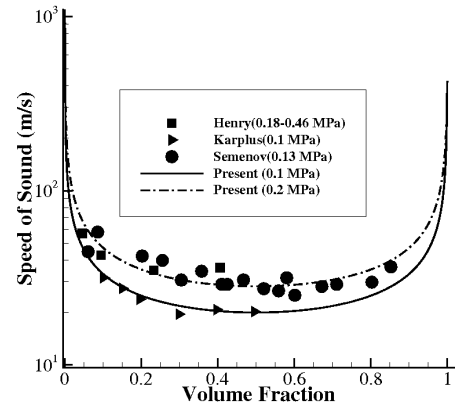

Figure 1: Comparison of speed of sound in water-vapor mixture with experiments.

Test filtering is defined by the linear interpolation from face values of a control volume, which is again the interpolation from two adjacent cell center values (Park and Mahesh (2007)):

$$\widehat{\phi} = \frac{1}{N_{\text{face}}}\sum_{\text{no of face}}\phi_f = \frac{1}{2N_{\text{face}}}\sum_{\text{no of face}}(\phi_{icv1}+\phi_{icv2}), \tag{11}$$

where N_{face} is the number of faces for a given control volume.

The expression for the speed of sound in a water-vapor mixture is obtained using the equation of state and Gibbs equation and is given by

$$\begin{aligned} a^2 &= \frac{C_1T}{C_0 - \dfrac{C_1}{C_{pm}}}, \text{where} \\ C_0 &= 1 - (1-Y)\rho K_lT\frac{P_c}{(p+P_c)^2}, \\ C_1 &= R_gY - K_l(1-Y)\frac{P}{p+P_c}, \\ C_{pm} &= YC_{pg} + (1-Y)C_{pl}. \end{aligned} \tag{12}$$

The change in speed of sound with gas volume fraction at a given temperature and pressure, obtained using the above relation is compared to experimental results (Henry et al. (1971); Semenov and Kosterin (1964); Karplus (1957)) in Figure 1. This speed is obtained assuming that there is no mass transfer between the phases and hence is not the equilibrium speed of sound. Note the good agreement with experiments; also the effect of vapor in changing the acoustic characteristics of water is evident. Note that the sound speed in the mixture ranges from 1480 m/s for pure water to 30 m/s for certain values of vapor volume fraction.

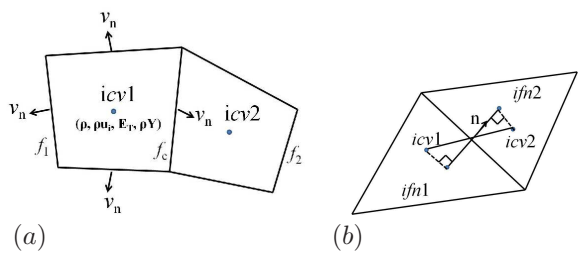

Figure 2: (a) Schematic of the collocated finite volume method, (b) Schematic for computation of face normal gradient for viscous terms.

In case of cavitating flows, S_e and S_c are source terms for evaporation of water and condensation of vapor and are given by

$$S_e = C_e \alpha^2 (1-\alpha)^2 \frac{\rho_l}{\rho_g} \frac{\max((\mathrm{p_v} - \mathrm{p}), 0)}{\sqrt{2\pi R_g T}}, \quad (13)$$

$$S_c = C_c \alpha^2 (1-\alpha)^2 \frac{\max((\mathrm{p_v} - \mathrm{p}), 0)}{\sqrt{2\pi R_g T}},$$

where α is the volume fraction of vapor and p_v is the vapor pressure. C_e and C_c are empirical constants. Saito et al. (2007) have shown that the source terms are not very sensitive to the values of these empirical constants and arrive at an optimum value of 0.1 for both the constants. Vapor pressure is related to temperature by

$$p_v = p_k \exp((1 - \frac{\mathrm{T_k}}{\mathrm{T}})(\mathrm{a} + (\mathrm{b} - \mathrm{cT})(\mathrm{T} - \mathrm{d})^2)), \quad (14)$$

where p_k = 22.130 MPa , T_k = 647.31 K , a = 7.21, b = 1.152 x 10^{-5}, c = -4.787 x 10^{-9}, d = 483.16.

NUMERICAL METHOD

The numerical method adopts a predictor corrector approach. In the predictor step, Eqs. (3) are discretized using a collocated, cell-centered finite volume method. Figure 2(a) illustrates the storage of variables and the notation used. The solution is first advanced using a non-dissipative predictor step. The characteristic based filter is then applied as a corrector.

Predictor step

A predicted value is first obtained by solving Eqs. (3) using a symmetric and non-dissipative scheme. The convective fluxes at the face are estimated using a symmetric average with a gradient term using Taylor's series expansion to give

$$\phi_{f_c} = \frac{\phi_{icv1} + \phi_{icv2}}{2} + \frac{1}{2}\left(\nabla\phi|_{icv1} \cdot \Delta\mathbf{x}^{icv1} + \nabla\phi|_{icv2} \cdot \Delta\mathbf{x}^{icv2}\right), \quad (15)$$

where $\Delta\mathbf{x}^{icv1} = \mathbf{x}_{f_c} - \mathbf{x}_{icv1}$, and $\nabla\phi|_{icv1}$denotes the gradient defined at $icv1$. The gradient is estimated using a modified least-square method (Park and Mahesh (2007)),

The viscous term is split into two parts, $\sigma_{ij} = \sigma^1_{ij} + \sigma^2_{ij}$, where $\sigma^1_{ij} = \frac{\mu}{Re}\frac{\partial u_i}{\partial x_j}$ and $\sigma^2_{ij} = \frac{\mu}{Re}\left(\frac{\partial u_j}{\partial x_i} - \frac{2}{3}\frac{\partial u_k}{\partial x_k}\delta_{ij}\right)$. σ^2_{ij} can be interpreted as a 'compressible' contribution, since it vanishes in the incompressible limit. The 'incompressible' component σ^1_{ij} is computed by

$$\frac{1}{V_{\mathrm{cv}}} \sum_{\mathrm{faces}} \left(\frac{\mu}{Re}\right)_f \left.\frac{\partial u_i}{\partial n}\right|_f A_f. \quad (16)$$

Here, the normal gradient at the face is computed by

$$\frac{\partial \phi}{\partial n} = \frac{\phi_{ifn2} - \phi_{ifn1}}{d_f}, \quad (17)$$

where $ifn1$ ($ifn2$) is the projection of $icv1$ ($icv2$) onto the extension of normal vector $\mathbf{n}$ and d_f is the distance between $ifn1$ and $ifn2$ as illustrated in Figure 2(b). ϕ_{ifn1} is given by

$$\phi_{ifn1} = \phi_{icv1} + \nabla\phi|_{icv1} \cdot (\mathbf{x}_{ifn1} - \mathbf{x}_{icv1}), \quad (18)$$

where the conventional least-square method is used to determine the gradient $\nabla\phi$ at $icv1$. Viscosity at the cell face is given by Eq. (15) and a least square reconstruction. Thus, the incompressible part corresponds to compact-stencil method. $\sigma^2_{ij,f}$ is constructed by the interpolation of $\sigma^2_{ij}\big|_{icv1}$ and $\sigma^2_{ij}\big|_{icv2}$ using Eq. (15).

Discrete positivity of viscous dissipation

The viscous term in the energy equation corresponds to the viscous dissipation term and by the second law of thermodynamics, should always remain positive. This term is therefore re-written to discretely ensure positivity.

$$\sigma_{ik}\frac{\partial u_i}{\partial x_k} = \frac{4}{3}[(\frac{\partial u}{\partial x})^2 + (\frac{\partial v}{\partial y})^2 + (\frac{\partial w}{\partial z})^2] + (\frac{\partial u}{\partial y} + \frac{\partial v}{\partial x})^2 + (\frac{\partial u}{\partial z} + \frac{\partial w}{\partial x})^2 + (\frac{\partial v}{\partial z} + \frac{\partial w}{\partial y})^2. \quad (19)$$

This sum of squares is strictly positive and hence viscous dissipation remains discretely positive at all times. This operation is also cheaper than forming the tensors and computing their scalar product.

Time advancement

A second-order explicit Adams-Bashforth scheme is used.

$$q_j^{n+1} = q_j^n + \frac{\Delta t}{2}\left[3\mathrm{rhs}_j(\mathbf{q}^n) - \mathrm{rhs}_j(\mathbf{q}^{n-1})\right], \quad (20)$$

where rhs_j denotes j^{th} component of the right hand side of the governing equation, and the superscript n denotes the nth time step.

Corrector step : Characteristic-based Filter

The predictor step described in the previous section is non-dissipative and hence cannot capture discontinuities (both shocks and material discontinuities). An external discontinuity capturing mechanism is therefore provided. Yee et al. (1999) developed a characteristic based filtering method for ideal gases on structured grids which was extended to ideal gases on unstructured grids by Park and Mahesh (2007). In this paper a characteristic based filtering method is developed for mixtures of fluids and non ideal gases on unstructured grids. Note that any time integration scheme can be used in the predictor step and it will not affect the implementation of the corrector step. Once a physical time step Δt is advanced to get the solution $\widehat{q}^{n+1}$ from q^n, the final solution q^{n+1} at $t + \Delta t$ is obtained from a corrector scheme

$$q_{cv}^{n+1} = \widehat{q}_{cv}^{n+1} - \frac{\Delta t}{V_{cv}} \sum_{\text{faces}} (F_f^* . n_f) A_f, \quad (21)$$

where F_f^* is the filter numerical flux of the following form

$$F_{fc}^* = \frac{1}{2} R_{fc} \Phi_{fc}^*. \quad (22)$$

Here R_{fc} is the right eigenvector vector at the face computed using Roe-average of the variables from left and right control volumes. The expression for the lth component of Φ^*, ϕ^{*l} is given by

$$\phi_{fc}^{*l} = k\theta_{fc}^l \phi_{fc}^l, \quad (23)$$

where k is an adjustable parameter and θ_{fc} is the Harten's switch function given by

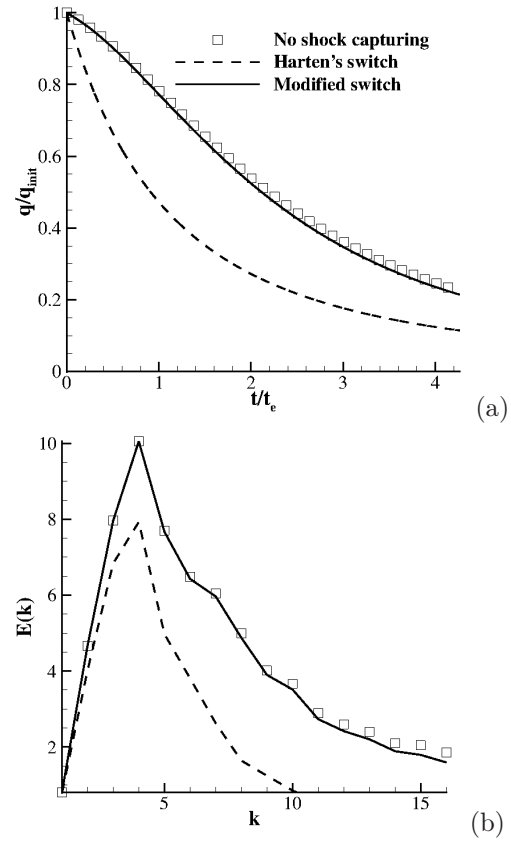

Figure 3: (a) Comparison of temporal decay of Kinetic energy obtained using original Harten's switch and modified singlephase switch with results obtained using no shock capturing, (b) Radial energy spectrum at $t/t_e = 4.0$ obtained using original Harten's switch and modified singlephase switch compared with results obtained using no shock capturing.

$$\begin{aligned} \theta_{fc} &= \sqrt{0.5(\widehat{\theta}_{icv1}^2 + \widehat{\theta}_{icv2}^2)}, \\ \widehat{\theta}_{icv1} &= \frac{|\beta_{fc}| - |\beta_{f1}|}{|\beta_{fc}| + |\beta_{f1}|}, \\ \widehat{\theta}_{icv2} &= \frac{|\beta_{f2}| - |\beta_{fc}|}{|\beta_{f2}| + |\beta_{fc}|}. \end{aligned} \quad (24)$$

Here, $\beta_f = R_f^{-1}(q_{icv2} - q_{icv1})$ is the difference between characteristic variables across the face. f_1 and f_2 in a structured grid are the face neighbors in the corresponding direction (i.e. in the direction of the face normal). This definition is not possible in an unstructured grid, hence the concept of most parallel faces was introduced in Park and Mahesh (2007). Figure 2(a) illustrates this concept. For ϕ^ℓ, the Harten-Yee TVD form is used as suggested by

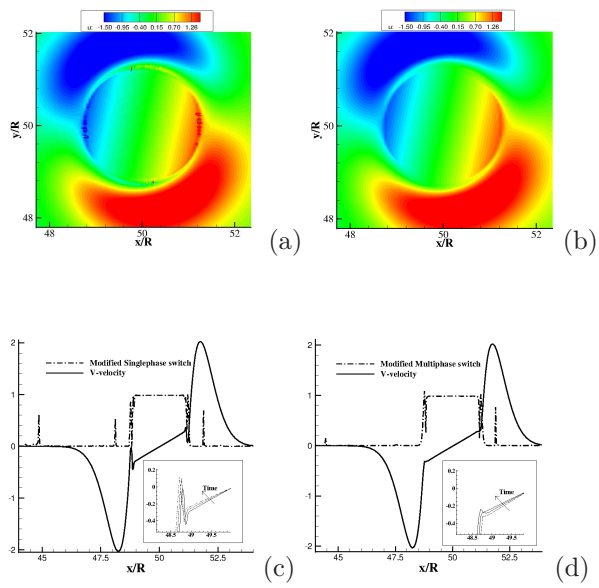

Figure 4: (a) and (b) Streamwise velocity contours for modified single phase and multiphase switch respectively, (c) Variation of modified singlephase switch and v-velocity along the $\theta = 0$ line, (d) Variation of modified multiphase switch and v-velocity along the $\theta = 0$ line.

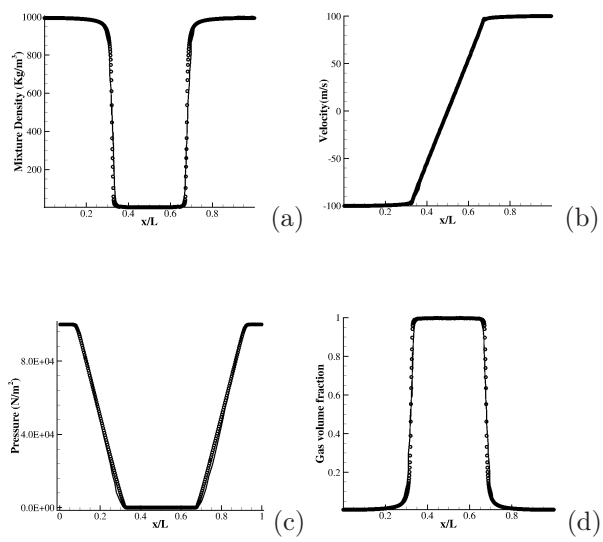

Figure 5: Comparison of present numerical results and numerical results of Saurel and Lemetayer (2001) for (a) density, (b) velocity, (c) pressure and (d) volume fraction of vapor. (▫) : Present, (—) : Saurel and Lemetayer (2001).

Yee et al. (1999).

$$\begin{aligned}\phi^{\ell}_{f_c} &= \frac{1}{2}\Psi\left(a^{\ell}_{f_c}\right)\left(g^{\ell}_{icv1}+g^{\ell}_{icv2}\right)-\Psi\left(a^{\ell}_{f_c}+\gamma^{\ell}_{f_c}\right)\beta^{\ell}_{f_c},\\ \gamma^{\ell}_{f_c} &= \frac{1}{2}\frac{\Psi\left(a^{\ell}_{f_c}\right)\left(g^{\ell}_{icv2}-g^{\ell}_{icv1}\right)\beta^{\ell}_{f_c}}{\left(\beta^{\ell}_{f_c}\right)^2+\epsilon},\end{aligned} \tag{25}$$

where $\epsilon = 10^{-7}$ and $\Psi(z) = \sqrt{\delta + z^2}$ $(\delta = 1/16)$ is introduced for the entropy fixing. $a^{\ell}_{f_c}$ is the element of the jacobian matrix. For a structured grid, the value of the limiter function g_{icv} can be defined at the cell centers using the value of α at faces. Defining this in an unstructured grid will require interpolation. To avoid this, we define g at the faces. This is more natural because Eqs. (25) require only symmetric average $\frac{1}{2}\left(g_{icv1}+g_{icv2}\right)$ and difference $\frac{1}{2}\left(g_{icv2}-g_{icv1}\right)$ of g between the neighboring control volumes. Thus the expression of g is given by

$$\begin{aligned}g^{+\ell}_{f_c} &\equiv \frac{1}{2}\left\{\text{minmod}\left(\beta^{\ell}_{f_1},\beta^{\ell}_{f_c}\right)+\text{minmod}\left(\beta^{\ell}_{f_c},\beta^{\ell}_{f_2}\right)\right\},\\ g^{-\ell}_{f_c} &\equiv \frac{1}{2}\left\{\text{minmod}\left(\beta^{\ell}_{f_2},\beta^{\ell}_{f_c}\right)-\text{minmod}\left(\beta^{\ell}_{f_1},\beta^{\ell}_{f_c}\right)\right\}.\end{aligned} \tag{26}$$

The expressions for $\phi^{\ell}_{f_c}$ and $\gamma^{\ell}_{f_c}$ can now be written as

$$\begin{aligned}\phi^{\ell}_{f_c} &= \Psi\left(a^{\ell}_{f_c}\right)g^{+\ell}_{f_c}-\Psi\left(a^{\ell}_{f_c}+\gamma^{\ell}_{f_c}\right)\beta^{\ell}_{f_c},\\ \gamma^{\ell}_{f_c} &= \frac{\Psi\left(a^{\ell}_{f_c}\right)g^{-\ell}_{f_c}\beta^{\ell}_{f_c}}{\left(\beta^{\ell}_{f_c}\right)^2+\epsilon},\end{aligned} \tag{27}$$

This approach avoids any interpolation between cell center and faces and hence, on Cartesian grids will be equivalent to the expression proposed for structured grids by Yee et al. (1999). In order to determine the eigenvectors of the system, the flux Jacobian matrix needs to be expressed. First the expression for pressure needs to be expressed in terms of solution variables $q_j = (\rho, \rho u_i, \rho E_T, \rho Y)$. Note that total energy is used here even though internal energy is solved in the predictor step, since jump conditions need to be obtained for conservative variables. Eq. (7), when expressed in terms of the solution variables q becomes

$$\begin{aligned}a &= C_{vl}(q_1-q_6)+C_{vg}q_6,\\ b &= C_{pl}P_c(q_1-q_6)+C_{vg}P_cq_6-\\ &\quad [(q_1-q_6)K_l+q_6R_g][q_5-0.5\frac{{q_2}^2+{q_3}^2+{q_4}^2}{q_1}],\\ c &= -q_6R_gP_c[q_5-0.5\frac{{q_2}^2+{q_3}^2+{q_4}^2}{q_1}].\end{aligned} \tag{28}$$

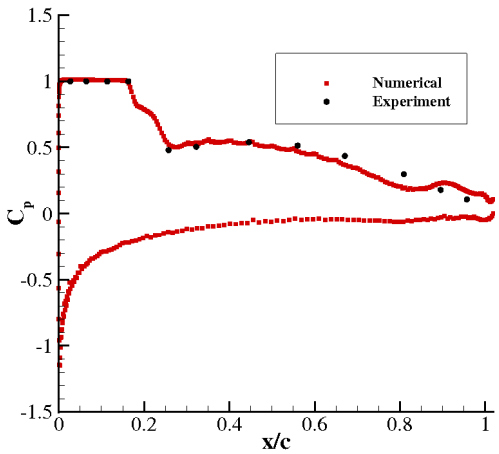

Figure 6: Comparison of C_p distribution with experiment.

$\dfrac{\partial p}{\partial q_j}$ is then obtained as

$$\frac{\partial p}{\partial q_j} = -\frac{[p^2 \dfrac{\partial a}{\partial q_j} + p\dfrac{\partial b}{\partial q_j} + \dfrac{\partial c}{\partial q_j}]}{2ap + b}. \tag{29}$$

Once the flux Jacobian matrix is obtained, the eigenvector vector matrix R_{ij} and its inverse R_{ij}^{-1} can be evaluated.

Modification of Harten's switch

Park and Mahesh (2007) showed that for a single phase flow, the original Harten's switch θ_{fc} proposed by Yee et al. (1999) is excessively dissipative. They make use of a temporally decaying isotropic turbulence problem to show that the original Harten's switch affects resolved turbulence and propose a modified switch based on divergence and vorticity. In order to evaluate the performance of this switch and the original Harten's switch in multiphase flows, we perform LES of decaying isotropic turbulence in a mixture of water and vapor. The simulation is performed on a coarse grid of 32^3 volumes with an initial Taylor micro scale Reynolds number $Re_\lambda = u_{rms}\lambda/\nu = 68.7$. The initial spectrum is given by

$$E(k) = 16\sqrt{\frac{2}{\pi}}\frac{u_0^2}{k_0}\left(\frac{k}{k_0}\right)^4 \exp\left(-2k^2/k_0^2\right), \tag{30}$$

and the initial fluctuation Mach number is 0.001. The pressure fluctuations are such that the flow does not cavitate. Even in the absence of any discontinuities, the Harten's switch is found to be dissipative

Figure 7: Mean void fraction contour for $\sigma = 1.0$.

thereby affecting the resolved turbulence as shown in Figure 3. Hence the Harten's switch θ_{f_c} is modified using a sensor based on Ducros switch (Ducros et al. (1999)) to prevent excessive dissipation.

$$\begin{aligned} \theta_{f_c} &= \theta_{f_c}\theta^\star_{f_c}, \\ \theta^\star_{f_c} &= \frac{1}{2}\left(\theta^\star_{icv1} + \theta^\star_{icv2}\right), \\ \theta^\star_{icv1} &= \frac{(\nabla\cdot\mathbf{u})^2_{icv1}}{(\nabla\cdot\mathbf{u})^2_{icv1} + \Omega^2_{icv1} + \epsilon}. \end{aligned} \tag{31}$$

Here Ω is the vorticity magnitude and $\epsilon = 10^{-7}$ is a small positive value. The modified switch, henceforth called as modified single phase switch, limits dissipation away from discontinuities. This is clearly seen in Figure 3 which shows kinetic energy (q) decay and the radial energy spectrum. t_e is the eddy turnover time. However, even this switch causes problems in a cavitating flow. Consider an inviscid cavitating vortex on a square domain of dimensions 100R x 100R. The initial velocity field is

$$\begin{aligned} u &= -\frac{C(y-y_c)}{R^2}\exp(-r^2/2) \text{ and} \\ v &= \frac{C(x-x_c)}{R^2}\exp(-r^2/2). \end{aligned} \tag{32}$$

Here $r^2 = ((x-x_c)^2 + (y-y_c)^2)/R^2$ and $R = 1$, $C = 5.0$, $x_c = y_c = 50R$. Constant density, pressure and temperature are specified initially. As the solution evolves, pressure in the center of the vortex drops below vapor pressure and the flow cavitates. As the vortex cavitates, the value of the modified singlephase switch becomes very small because of the large vorticity there. Hence numerical oscillations are encountered as shown Figure 4(a). Figure 4(c) shows the variation of v-velocity and the modified singlephase switch along the $\theta = 0$ line. Note the oscillation in v-velocity and the very small value of the switch at the corresponding location. This oscillation increases with time and causes the solution to become unstable. As a remedy, an additional term is added to the modified single phase switch.

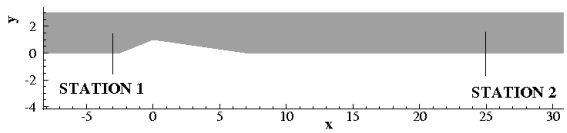

Figure 8: Geometry and computational domain for wedge.

$$\theta^{\star}_{f_c} = \frac{1}{2}\left(\theta^{\star}_{icv1} + \theta^{\star}_{icv2}\right) + \left|\left(\alpha_{\mathrm{icv2}} - \alpha_{\mathrm{icv1}}\right)\right| \qquad (33)$$

This additional term prevents the switch from reaching very small values inside the cavitating vortex. Note that the additional term automatically goes to zero in single phase regions and hence termed as modified multiphase switch. Its effect is clearly seen in Figure 4(b) in terms of an oscillation-free solution. Figure 4(d) shows that the proposed modification prevents the switch from reaching very small values inside the vortex. When applied to the turbulent problem discussed above, it yields identical results to the form proposed by Park and Mahesh (2007).

RESULTS

We evaluate the proposed algorithm for two types of cavitating flows. In subsection "Validation" a one dimensional cavitating problem and a turbulent cavitating flow over a hydrofoil are discussed. Finally, the algorithm is applied to perform LES over a wedge in Section "LES of sheet cloud cavitation over a wedge".

Validation

The first test problem is a one dimensional tube consisting of water initially at atmospheric pressure and two streams moving away from the center at 100 m/s. This problem has been previously investigated by many authors (Saurel and Lemetayer (2001); Liu et al. (2004); Barberon and Helluy (2005)). We compare our results with the results obtained using a multi fluid approach by Saurel and Lemetayer (2001). The expansion at the center causes a vapor bubble to be produced as soon as the pressure reaches vapor pressure. Thus two interfaces are created dynamically due to the rarefaction waves. The mixture density, pressure, velocity and vapor volume fraction at the end of 1860μs are compared with numerical results from Saurel and Lemetayer (2001) and the results agree very well with each other.

Table 1: Flow parameters in experiment and simulation

		Experiment	Simulation
Station 1:	σ	1.9	2.4
Station 2:	Pressure	52 KPa	70 KPa

Next, we consider a turbulent cavitating flow over a hydrofoil. The hydrofoil section used is NACA 66(mod) with a camber ratio of 0.02 and a thickness ratio of 0.09. The Reynolds number based on chord length is 2 $\times 10^6$, the angle of attack is 4 degrees and the cavitation number $\sigma = \frac{p_\infty - p_v}{0.5\rho_\infty u_\infty^2}$ is 1.0. At this cavitation number a leading edge cavitaty is observed. Others (Leroux et al. (2004); Laberteaux and Ceccio (2001)) also refer to this as partial sheet cavity and open cavity. Shen and Dimotakis (1989) conducted experiments on this hydrofoil and our numerical results are compared against their experimental results. We use a Spallart Allmaras turbulence model for this case. Figure 6 shows the time averaged pressure coefficient distribution along the chord for both the suction and pressure side. The results agree well with the experimental results. Experiments observed that the partial cavity closure oscillated about its mean position and our numerical results also showed such oscillations. Figure 7 shows the mean void fraction contour showing the presence of a sheet cavity near the leading edge. This result also agree with the conclusions of Leroux et al. (2004), that a quasi-stable partial sheet cavity is formed for cavity lengths less than half the chord length.

LES of sheet to cloud cavitation over a wedge

For sheet to cloud cavitation, a wedge geometry is considered. Experiments are being conducted on this geometry at the University of Michigan and the results presented here are a part of the numerical investigation being carried out to match the experimental results. The experimental setup has a contraction leading to a test section of square cross section (1 inch). For the sake of simplicity, the contraction is avoided in the simulation and is replaced by a constant area section as shown in Figure 8. Further, the domain is extended in both upstream and downstream directions. The simulation attempts to match the cavitation number at station 1 and pressure at station 2 marked in Figure 8. The Reynolds number based on the maximum wedge height (1 inch) and a bulk velocity of 7.9 m/s is approximately 0.2 $\times 10^6$. Table 1 lists the rele-

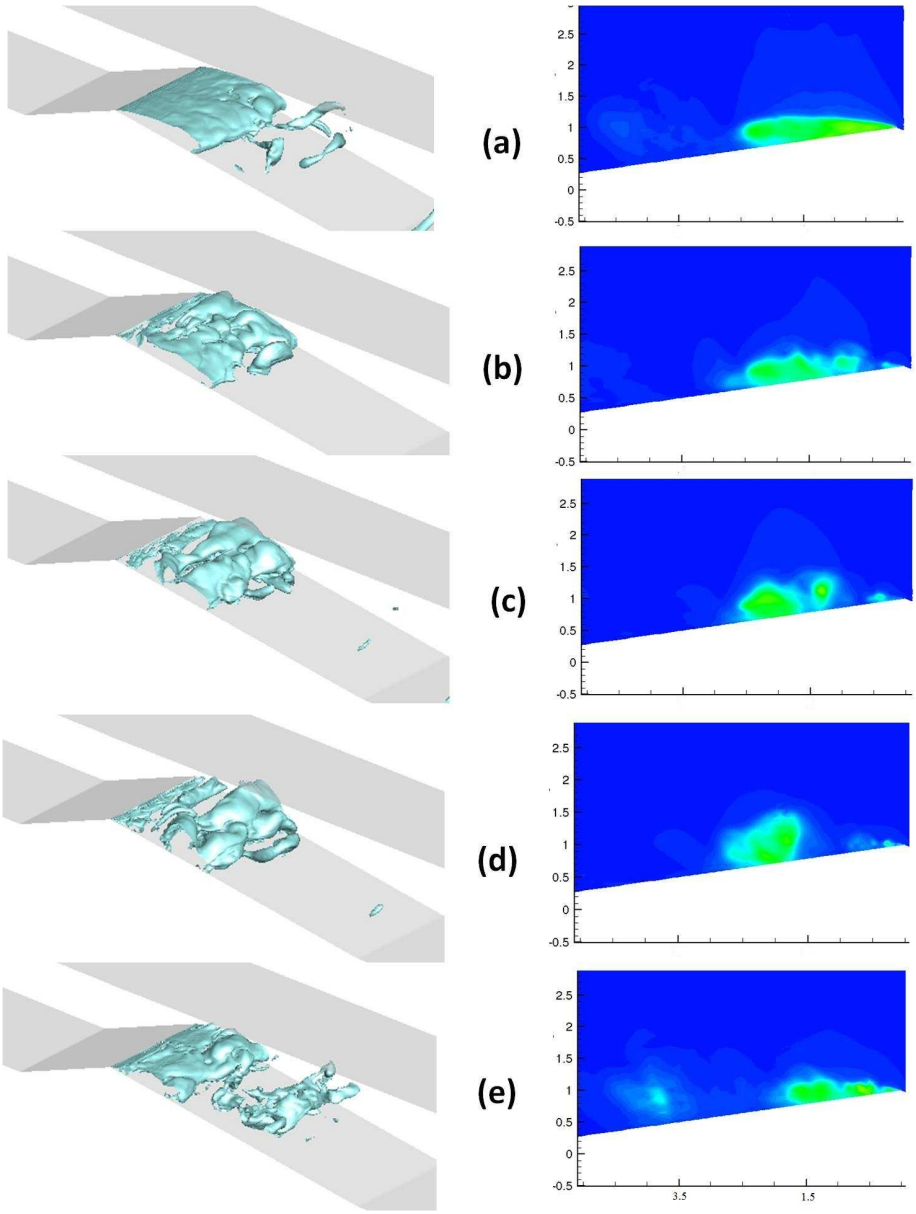

Figure 9: Time series of evolution of cavity and destabilization leading to a cloud.

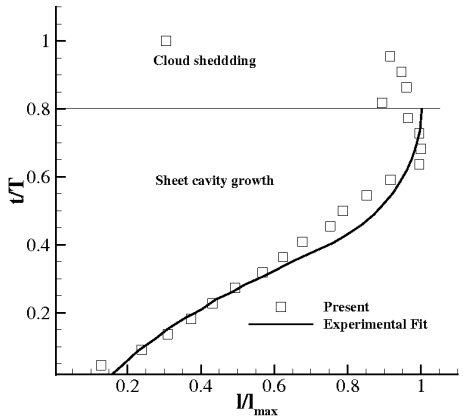

Figure 10: Variation of non-dimensional cavity length with time in one cycle.

vant values at both the stations in experiment and simulation. Sponge boundary conditions are implemented both upstream and downstream of the wedge to minimize reflections from the boundaries. No slip boundary condition is imposed on top and bottom wall. A periodic boundary condition is enforced in the spanwise boundaries for the current simulation as opposed to side walls.

Figure 9 shows the series of events in time. The figures on the left are the isocontours of void fraction showing the three dimensional nature of the phenomenon. The figures on the right are the corresponding span averaged void fraction contours. A fully formed cavity first develops up to a length x/h = 2.6, where h is the height of the wedge. The cavity then pinches off, then rolls up into a cloud which then sheds off from the main cavity. At the instant of the cavity detachment, the length of the attached cavity is very small and a new attached sheet cavity starts forming from the wedge apex. The detached cloud meanwhile collapses giving rise to large scale pressure fluctuations. Small secondary cloud shedding can be observed from the three dimensional isocontours and this occurs just before the main cloud sheds.

The Strouhal number corresponding to this instability $St = \frac{fl_{max}}{U_{inf}}$ is about 0.3, which lies within the acceptable range of 0.2 - 0.4. Here, l_{max} is the maximum mean length of the cavity and U_{inf} is the free stream velocity just before the apex of the wedge. The cavity length obtained at various time instants is compared with experimental data of Callenaere et al. (2001) in Figure 10. Here, the length of the cavity (l) plotted along the abscissa is normalized using the maximum cavity length ($l_{max}/h = 2.6$) and the time (t) is normalized using the time period of the entire cycle(T), which is about 17ms for this case. The sheet cavity grows up to its maximum length until about 0.8T. Then it oscillates around the maximum length from 0.8T-0.9T. During this time a small secondary cloud is shed, which is not normally captured in time averaged simulations (Seo and Lele (2009)). Leroux et al. (2004) have observed these secondary cloud shedding in a hydrofoil geometry. Then an abrupt change in cavity length is observed when the cloud pinches off from the main cavity at $l/l_{max} = 0.2$.

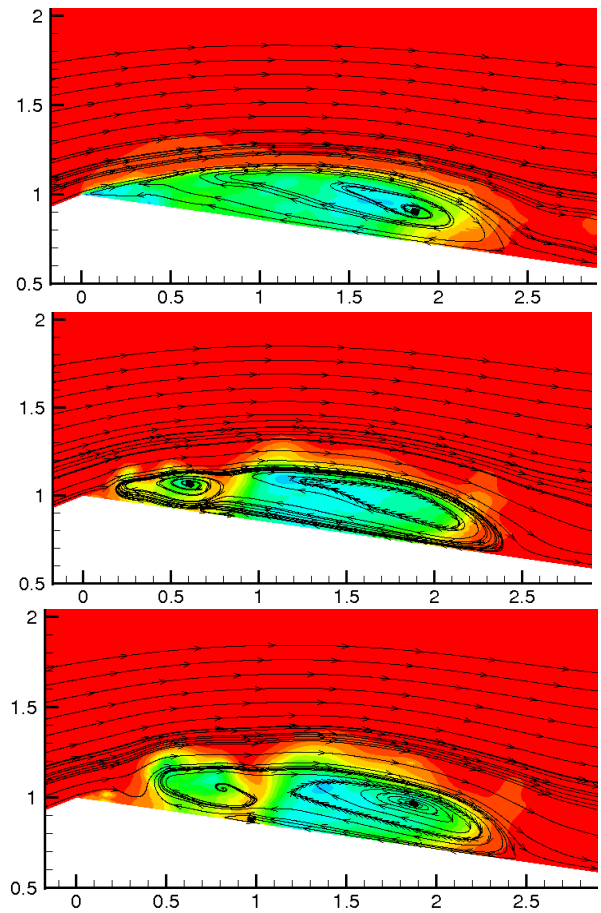

Figure 11: Visualization of re-entering jet at different time instants during sheet to cloud transition.

For visualizing the re-entering jet, span averaged values are considered. Although some span wise variation in re-entering jet is present, this method will give us details about the mean behavior. Streamlines plotted at 0.85T , 0.90 T and 0.98T are shown in Figure 11 and it shows the presence of a re-entering jet where a stream of liquid from the cavity closure enters into the cavity. This interaction also causes a small secondary cloud to shed. The re-

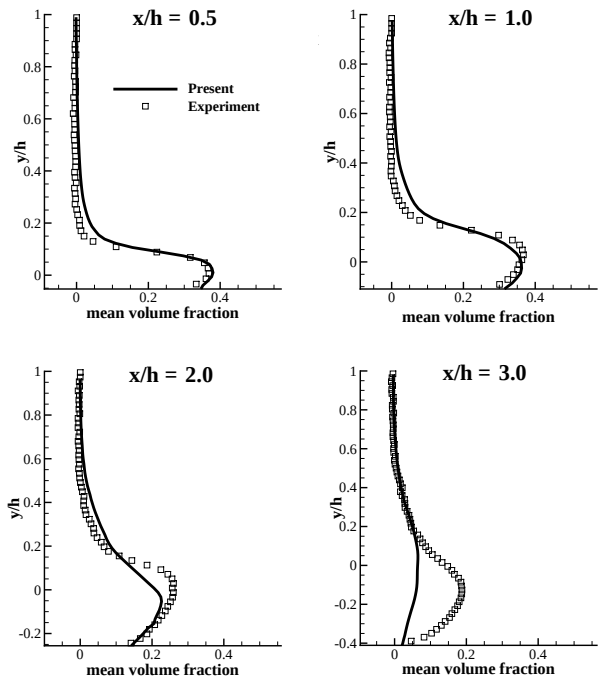

Figure 12: Comparison of average volume fraction with experimental values at different streamwise locations. Experimental data provided by Prof. Ceccio (private communication).

entrant jet then penetrates towards the apex of the wedge and the cavity pinches off close to the apex of the wedge. The mean volume fraction values at various streamwise locations are compared with X-ray measurements from the experiment. Very good agreement is observed for $x/h = 0.5$ and $x/h = 1.0$, while some differences appear for the downstream locations. This is because of the fact that the size of the mean vapor cavity in the simulation is smaller than that in the experiment. This is consistent with flow conditions of the simulation where both the upstream cavitation number and the downstream pressure are higher than that of the experimental values. Simulations are currently underway to better match the conditions with the experiment and it is expected that the comparison in the downstream locations will get better.

Figure 13 shows instantaneous isocontours of Q-criterion(Q = 5), colored with streamwise velocity. Note the three dimensionality of the flow and the range of scales. The structures appear more coherent close to the apex, due to the low Reynolds number nature of the flow there. Hairpin shaped structures that were observed in the experiments can be observed in the numerical simulations too. Detailed statistics of intensities near the cavity will shed light on the effect of turbulence on the sheet to cloud mechanism. The extraction of this data is currently underway.

SUMMARY

A numerical method using characteristic-based filtering developed to simulate multiphase and cavitating flows is used to perform Large Eddy Simulation of cavitation. A homogeneous equilibrium model is used to model the multiphase mixture as a single compressible fluid. A characteristic-based filter developed for multiphase flows is applied in a predictor corrector method to make it independent of the base scheme. A sensor based on vorticity, divergence and volume fraction is used to prevent excessive dissipation away from the discontinuities. The method is validated using a one dimensional cavitating tube and a partial cavitation over a NACA hydrofoil. Reasonable agreement is obtained with the available experimental data. The method is used to perform LES of sheet to cloud cavitation over a wedge geometry. A re-entering jet of liquid is found to be responsible for the sheet to cloud transition. The length of the partial sheet cavity at various time instants agrees very well with the available experimental results. Three dimensional hairpin shaped structures observed in experiments are also seen in the present numerical simulations. Detailed investigation of the effect of turbulence on sheet to cloud mechanism is currently being performed.

ACKNOWLEDGMENT

This work was supported by the United States Office of Naval Research under ONR Grant N00014-11-1-0497 with Dr. Ki-Han Kim as the program manager. Computing resources were provided by the Arctic Region Supercomputing Center of HPCMP and the Minnesota Supercomputing Institute. The authors also thank Prof. Steven Ceccio, University of Michigan for providing the experimental data.

References

Arndt, Roger EA, Song, CCS, Kjeldsen, M, He, J, and Keller, A. "Instability of partial cavitation: a numerical/experimental approach". Twenty Third Symposium on Naval Hydrodynamics, 2000.

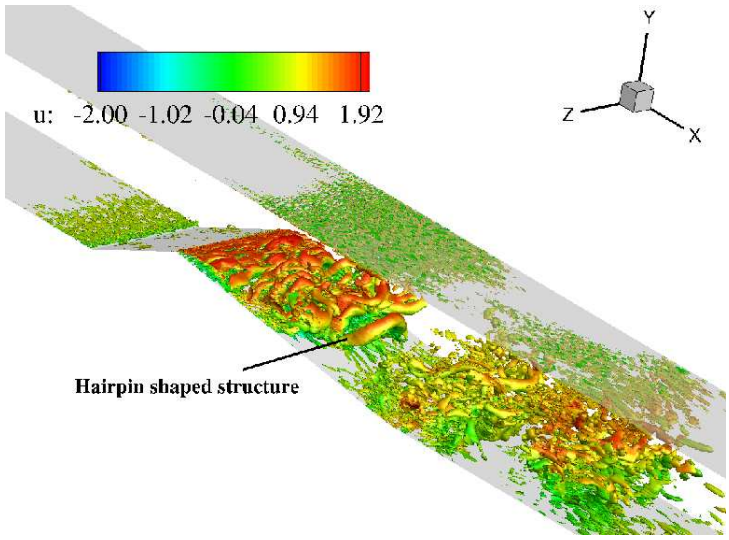

Figure 13: Isocontours of Q-criterion colored with streamwise velocity showing hairpin shaped structures.

Barberon, Thomas and Helluy, Philippe. "Finite volume simulation of cavitating flows". Computers & fluids, 34(7):832–858, 2005.

Callenaere, Mathieu, Franc, Jean-Pierre, MICHEL, JEAN, and Riondet, Michel. "The cavitation instability induced by the development of a reentrant jet". Journal of Fluid Mechanics, 444:223–256, 2001.

Coquel, F, El Amine, K, Godlewski, E, Perthame, B, and Rascle, P. "A numerical method using upwind schemes for the resolution of two-phase flows". Journal of Computational Physics, 136(2): 272–288, 1997.

Ducros, F, Ferrand, V, Nicoud, F, Weber, C, Darracq, D, Gacherieu, C, and Poinsot, T. "Large-eddy simulation of the shock/turbulence interaction". Journal of Computational Physics, 152(2): 517–549, 1999.

Ghosh, Shankar and Mahesh, Krishnan. "Numerical simulation of the fluid dynamic effects of laser energy deposition in air". Journal of Fluid Mechanics, 605(1):329–354, 2008.

Henry, Robert E, Grolmes, MA, and Fauske, Hans Kare. "Pressure-pulse propagation in two-phase one-and two-component mixtures.". Technical report, Argonne National Lab., Ill., 1971.

Hirt, Cyril W and Nichols, Billy D. "Volume of fluid (vof) method for the dynamics of free boundaries". Journal of computational physics, 39(1):201–225, 1981.

Karplus, Henry B. "Velocity of sound in a liquid containing gas bubbles". The Journal of the Acoustical Society of America, 29:1261, 1957.

Kubota, Akihiro, Kato, Hiroharu, and Yamaguchi, Hajime. "A new modelling of cavitating flows: A numerical study of unsteady cavitation on a hydrofoil section.". Journal of fluid Mechanics, 240 (1):59–96, 1992.

Laberteaux, KR and Ceccio, SL. "Partial cavity flows. part 1. cavities forming on models without spanwise variation". Journal of Fluid Mechanics, 431:1–41, 2001.

Leroux, Jean-Baptiste, Astolfi, Jacques André, and Billard, Jean Yves. "An experimental study of unsteady partial cavitation". Journal of Fluids Engineering, 126(1):94–101, 2004.

Liu, TG, Khoo, BC, and Xie, WF. "Isentropic one-fluid modelling of unsteady cavitating flow". Journal of Computational Physics, 201(1):80–108, 2004.

Osher, Stanley and Fedkiw, Ronald P. "Level set methods: an overview and some recent results". Journal of Computational physics, 169(2):463–502, 2001.

Osher, Stanley and Fedkiw, Ronald P. "Level set methods". Geometric Level Set Methods in Imaging, Vision and Graphics. eds. S. Osher and N. Paragios, Springer-Verlag, NY, pages 3–20, 2003.

Park, Noma and Mahesh, Krishnan. "Numerical and modeling issues in les of compressible turbulence on unstructured grids". AIAA 2007, 722, 2007.

Popinet, Stéphane and Zaleski, Stéphane. "A front-tracking algorithm for accurate representation of surface tension". International Journal for Numerical Methods in Fluids, 30(6):775–793, 1999.

Saito, Yoshinori, Takami, Rieko, Nakamori, Ichiro, and Ikohagi, Toshiaki. "Numerical analysis of unsteady behavior of cloud cavitation around a naca0015 foil". Computational Mechanics, 40(1): 85–96, 2007.

Saurel, Richard and Abgrall, Rémi. "A multiphase godunov method for compressible multifluid and multiphase flows". Journal of Computational Physics, 150(2):425–467, 1999.

Saurel, Richard and Lemetayer, Olivier. "A multiphase model for compressible flows with interfaces, shocks, detonation waves and cavitation". Journal of Fluid Mechanics, 431(6):239–271, 2001.

Semenov, NI and Kosterin, SI. "Results of studying the speed of sound in moving gas-liquid systems". Teploenergetika, 11(6):46–51, 1964.

Seo, J and Lele, S. "Numerical investigation of cloud cavitation and cavitation noise on a hydrofoil section". 2009.

Seo, Jung H, Moon, Young J, and Shin, Byeong Rog. "Prediction of cavitating flow noise by direct numerical simulation". Journal of Computational Physics, 227(13):6511–6531, 2008.

Shen, Y and Dimotakis, Paul E. "The influence of surface cavitation on hydrodynamic forces". 1989.

Unverdi, Salih Ozen and Tryggvason, Grétar. "A front-tracking method for viscous, incompressible, multi-fluid flows". Journal of computational physics, 100(1):25–37, 1992.

Yee, Helen C, Sandham, Neil D, and Djomehri, MJ. "Low-dissipative high-order shock-capturing methods using characteristic-based filters". Journal of Computational Physics, 150(1): 199–238, 1999.

Youngs, DL. "Time-dependent multi-material flow with large fluid distortion". Numerical methods for fluid dynamics, 24:273–285, 1982.

All in-text references underlined in blue are linked to publications on ResearchGate, letting you access and read them immediately.